CHEMISTRY OF MATERIALS

pubs.acs.org/cm

Article

Zircon Structure as a Prototype Host for Fast Monovalent and Divalent Ionic Conduction

Qian Chen, Dogancan Sari, Ann Rutt, Jiyoon Kim, Gerbrand Ceder, and Kristin A. Persson*

Cite This: https://doi.org/10.1021/acs.chemmater.3c00902

Read Online

ACCESS | Metrics & More | Article Recommendations | Supporting Information

ABSTRACT: "Beyond Li-ion" energy storage solutions based on ions such as Na, Mg, Ca, and Zn have attracted increasing attention due to growing concerns about the cost, resource availability, and safety of the currently dominant Li-ion batteries. One of the greatest challenges for beyond-Li systems, especially multivalent ones, is the lack of materials with high ionic mobility. In this study, we find that zircon-type YPO_4 presents a unique structural environment that enables superior conduction of multiple species including Na^+, Ca^{2+}, Mg^{2+}, and Zn^{2+}, even in the dilute carrier concentration regime. This highly unusual capability originates from one-dimensional (1D) percolating channels of adjacent, distorted octahedral sites, which results in a smoothly varying coordination environment and correspondingly low activation barriers. Low decomposition energy of multiple compositions of doped YPO_4, where the carrier ions are introduced into the system along with subvalent doping into P sites, confirmed good stability and synthesizability. Among these compositions, we found $Na_{0.0625}YSi_{0.0625}P_{0.9375}O_4$ exhibiting good Na^+ conductivity of 0.99 mS/cm at 300 K with an activation energy of 220 meV. Zircon-structured $Na_{0.05}YSi_{0.05}P_{0.95}O_4$ was successfully synthesized; however, the highest density achieved (78%) was insufficient to conclusively establish its conductivity. Finally, we identify dopant−carrier association in doped YPO_4 as a key challenge for long-range diffusion in this structure family.

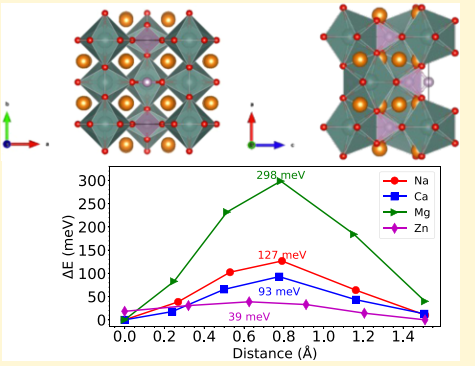

INTRODUCTION

Li-ion batteries (LIBs) are currently dominating the electric energy storage market with their high energy density and reliable performance.[1] However, growing concerns about the cost and resource availability for the projected 10-fold increase of the energy storage market are prompting the community to explore alternatives for future, next-generation batteries, i.e., "beyond Li-ion" technologies. Hence, rechargeable metal-ion batteries based on other ions such as Na^+, Ca^{2+}, Mg^{2+}, and Zn^{2+} are attracting increased research interest.[2−8]

Electrochemical energy storage inherently relies on the transport of charge carriers, which motivates the design and discovery of materials with frameworks with intrinsic high conductivity. For solid inorganic ionic conductors, it is well established that ionic mobility depends strongly on the crystal structure framework and the coordination preference of the mobile ion.[9,10] Despite the significant research progress made on identifying optimal structure frameworks for fast Li^+ conductors,[11−15] frameworks that are able to host and conduct a variety of non-Li carrier species are still very rare. In particular, multivalent carriers often exhibit different conduction pathways and usually higher diffusion barriers compared to Li in the same framework due to the change in preferred coordination environments, ionic radii, and electrostatic interactions.[16,17]

A few notable exceptions exist, e.g., within the β-alumina, NASICON, and Chevrel families of structures. The β-alumina family, one of the earliest reported solid-state electrolytes, has been shown to conduct a wide range of monovalent ions such as Na^+, Ag^+, K^+, Rb^+, and Li^+[18] as well as a conductivity of 10^{-3} mS/cm at 40 °C for divalent ions.[19,20] The good ionic conductivity across multiple cations has been attributed to the specific β-alumina structure, where conduction planes are formed between spinel blocks that accommodate two-dimensional mobility for multiple species. Similar features are found in layered oxides and sulfides such as V_2O_5,[21−23] MoO_3,[24−26] and TiS_2,[27−29] where diffusion channels for a variety of cations are observed in large interlayer spaces. Shortly after the discovery of β-alumina conductors, the NASICON-type framework with high Na^+ conductivity was reported,[30] which later was also found to support conduction of divalent ions like Mg^{2+}, Ca^{2+}, and Zn^{2+} at high temperatures (on the order of 1 mS/cm at 800 °C)[31,32] within interconnected large interstitial voids. The discovery of the NASICON-type conductors led to studies on a variety of compositions in the family as promising materials for both monovalent[33] and multivalent batteries.[34−36]

Received: April 16, 2023
Revised: July 7, 2023

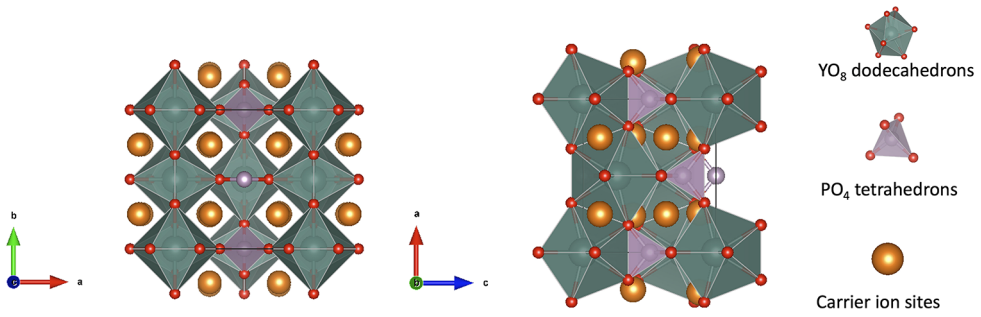

Figure 1. Crystal structure of zircon-type YPO_4 (space group: *I*41/*amd*) with carrier ion sites. The orange spheres show the sites where carrier ions can occupy.

Chevrel-phase $M_xMo_6T_8$ (T = S, Se, or Te), where mobile monovalent or divalent cations $M^{+/2+}$ can occupy the cavities between Mo_6T_8 blocks, provides a conduction framework for a broad range of ionic species including Li^+, Mg^{2+}, Ca^{2+}, Cd^{2+}, Zn^{2+}, Cu^+, Ni^{2+}, Mn^{2+}, Al^{3+}, etc.[37−40] Specifically, their excellent Mg^{2+} mobility has raised great interests as a potential candidate for Mg-ion batteries, despite their limited energy density.[41] Both NASICON and Chevrel share common crystal structure features such as connected spacious voids that enable multispecies conduction. However, in most materials, the multivalent ion conduction is still insufficient to meet the criteria for practical applications, i.e., a migration barrier lower than 650 meV[17] or a conductivity higher than 1 mS/cm at room temperature[10] for battery operations.

In this work, we present a new family of structures that are predicted to not only host and conduct multiple carrier ions but also provide fast conduction. Using first-principles calculations, we demonstrate unprecedented low migration barriers along percolating one-dimensional (1D) channels for both monovalent cations Na^+ and divalent cations Mg^{2+}, Ca^{2+}, and Zn^{2+} in YPO_4, which presents a zircon-type crystal framework. Furthermore, in contrast to many known Li-ion conductors in which the fast conduction is activated at high Li ion concentrations,[15,42,43] the zircon framework is predicted to exhibit fast ionic mobility even in the dilute carrier regime (less than 0.1 per formula unit), rendering it less sensitive to resource constraints. Zircon compounds can be described by general formula ABO_4 with a rich variety of compositions.[44] The zircon-type structure (space group: *I*41/*amd*) is formed with edge-sharing alternating AO_8 dodecahedrons and BO_4 tetrahedrons (Figure 1). Voids between these edge-sharing AO_8−BO_4 chains form open channels along the *c*-axis, where interstitials can be introduced.[45−47] The conduction of Li^+, Na^+, Mg^{2+}, and Ca^{2+} in zircon-type YPO_4 was experimentally observed in an early study[48] with M_3PO_4 (M = Li, Na) or $M_{1.5}PO_4$ (M = Mg, Ca) doped into the system. The results showed a Li conductivity of 3.7×10^{-2} S/cm and a Ca conductivity of 1.2×10^{-3} S/cm at 600 °C. However, the cation conduction mechanism was not established. In addition, as YPO_4 is also a protonic conductor,[49] the measured conductivity under ambient atmosphere can be mixed protonic/cation conduction. Using the charge-density-based cation insertion algorithm of Shen et al.,[50] we identified empty channels of interlocking, distorted octahedral sites, as shown in Figure 1. These sites are symmetrically equivalent, and the intersite distance is very short, about 1.5 Å, a unique feature of this structural family. Recently multiple compositions in this material family were proposed as cathode materials for Mg-ion batteries, showing reversible cycling in electrochemical tests and extremely favorable intrinsic mobility for Mg.[51]

In this work, the conduction of multiple mobile species including Na^+, Ca^{2+}, Mg^{2+}, and Zn^{2+} in pristine and doped YPO_4 is investigated through first-principles calculations. Nudged elastic band calculations show very low diffusion barriers for Na/Ca/Mg/Zn in pristine YPO_4, and ab initio molecular dynamics simulations confirm the 1D percolating diffusion channel in the zircon-type framework. We examine the phase stability and the defect formation of doped compositions when both carrier ion and subvalent dopants are introduced into the system and confirm good stability through low decomposition energy of compositions with different carrier−dopant combinations. Out of all examined compositions, Si-doped YPO_4 shows a high Na^+ estimated conductivity of 0.99 mS/cm at 300 K. Zircon-structured $Na_{0.05}YSi_{0.05}P_{0.95}O_4$ was successfully synthesized through a solid-state synthesis route; however, the highest density achieved (78%) of the resulting cold-pressed pellet is insufficient to conclusively establish its conductivity. Finally, to guide future explorations into the zircon conductor family, we investigate the dopant−carrier association behaviors in doped compositions.

METHODS

Density Functional Theory Calculations. Density functional theory (DFT) calculations were performed using the Vienna Ab initio Simulation Package (VASP)[52] within the projector augmented wave (PAW) approach[53] with the Perdew−Burke−Ernzerhof (PBE) generalized gradient approximation (GGA) functional.[54] For calculations with charged carrier ions in pristine YPO_4, a uniform compensating background charge was applied to maintain the charge neutrality.

Mobile Ion Site and Path Finding. The initial guess of mobile ion site positions was suggested based on the calculated local minima of the electronic charge density of the host structure.[50] DFT structure relaxations were performed to identify the most stable insertion site with the lowest total energy. The mobile ion migration graphs were constructed based on topological graph-based analysis developed by Shen et al.[55] to identify periodic continuous pathways in the framework. The identified connected hops were used for the following migration barrier calculations.

Phase Stability and Defect Formation Energy Calculations. The M^{3+} or M^{4+} ions were substitutionally doped into P sites (Wyckoff position 4*a*), and the carrier ions were inserted accordingly to maintain overall charge neutrality. To account for possible orderings when multiple carriers/dopants were present, for each composition, up to 50 symmetrically distinct atomic configurations with the lowest Ewald summation, as implemented in Pymatgen,[56] were generated. The total energy for each configuration was calculated from DFT, and the configuration with the lowest energy

https://doi.org/10.1021/acs.chemmater.3c00902
Chem. Mater. XXXX, XXX, XXX−XXX

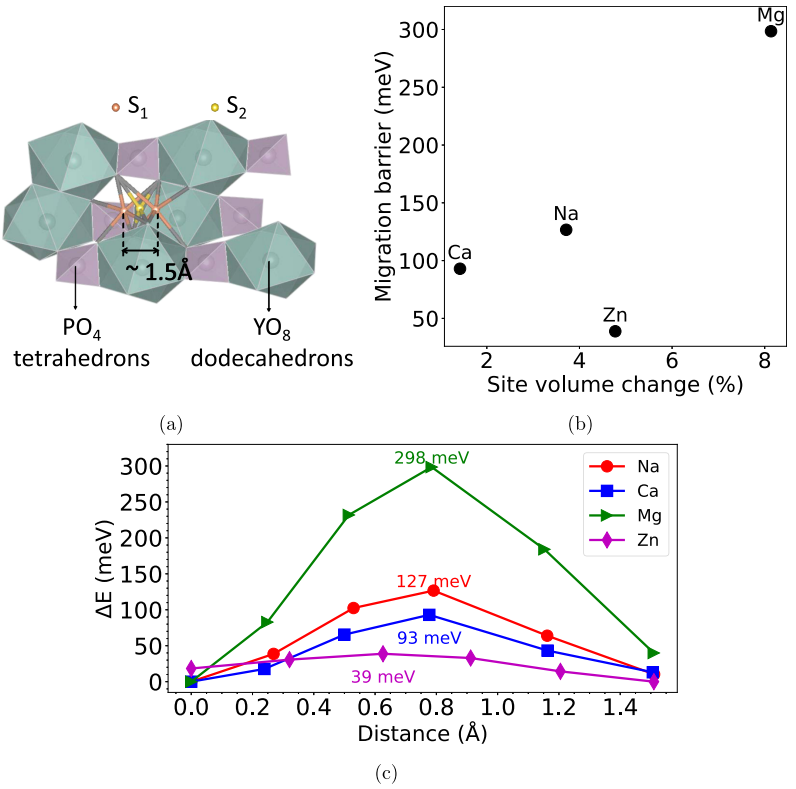

Figure 2. (a) Migration pathway of the carrier ion in YPO_4 in the channel along the *c*-axis. S_1 and S_2 show the end and intermediate positions of the carrier ion hop, respectively. Teal and purple polyhedrons represent YO_8 dodecahedrons and PO_4 tetrahedrons, respectively. (b) Migration barrier versus the site volume percentage change from the stable state (S_1) to the intermediate state (S_2). (c) Energy along the minimum energy migration pathway from S_1 to a neighboring S_1.

was used for subsequent calculations such as structure relaxation, nudged elastic band, and molecular dynamics simulations.

The total energy for each doped composition was calculated with input parameters consistent with the parameters used in the Materials Project (MP) database,[57] such as a plane-wave energy cutoff of 520 eV and a *k*-point mesh with a minimal density of 1000 per reciprocal atom. The energies of stable phases in the A−M−Y−P−O phase space were obtained from the MP database.[57] The thermodynamic stability of doped $A_xYM_yP_{1-y}O_4$ was assessed with the convex hull approach.[58]

The defect formation energy is calculated as

$$E_f^D = E_{tot}^D - E_{tot}^{pristine} - \sum_i n_i\mu_i \quad (1)$$

where E_{tot}^D and $E_{tot}^{pristine}$ are the total energies of the supercell with and without the defect, respectively. n_i is the number of atoms of specie *i* added to or removed from the supercell, and μ_i is the chemical potential of *i*. In the case of $A_xYM_yP_{1-y}O_4$, the formation energy of the defect complex consisting of one carrier ion interstitial A_i and one substitution M_P is calculated as

$$E_f^D = E_{tot}^D - E_{tot}^{pristine} - \mu_A - \mu_M + \mu_P \quad (2)$$

The chemical potentials are determined as the potential set corresponding to the multiphase equilibrium containing $A_xYM_yP_{1-y}O_4$ based on the A−M−Y−P−O phase diagram. To simulate the dilute limit, the defect formation energy is calculated using 2 × 2 × 3 supercells of the conventional unit cell (48 formula units) with one A_i−M_P pair.

Nudged Elastic Band Calculations. The minimum energy path of carrier hops between the two adjacent carrier ion sites was investigated using climbing-image nudged elastic band (CI-NEB) calculations.[59,60] NEB calculations were conducted for 2 × 2 × 2 supercells consisting of 96 atoms in the host structure and a single interstitial carrier ion. A plane-wave energy cutoff of 520 eV and a Γ-centered 2 × 2 × 2 *K*-mesh were used. The forces were converged to within 0.02 eV/Å.

Ab Initio Molecular Dynamics Simulations. Ab initio molecular dynamics (AIMD) simulations based on DFT were performed for 2 × 2 × 2 supercells in the temperature range of 700−1200 K. Non-spin-polarized calculations were performed with a plane-wave energy cutoff of 400 eV and a Γ-centered 1 × 1 × 1 *k*-point mesh. For AIMD calculations without a background charge, the lattice parameters were determined based on an NPT ensemble run of 3 ps for all temperatures. For those with a background charge, the volume of the cell was determined based on the equation of state using workflows implemented in mpmorph.[61] The production runs with the NVT ensemble were performed with the trajectory length ranging from 200 to 400 ps. The time step is 2 fs.

The diffusivity was obtained through a linear fitting of mean-squared displacement (MSD) of carrier ions over a duration time of *t*

$$D = \frac{1}{6}\frac{d\langle MSD\rangle}{dt} \quad (3)$$

The activation energy E_a was calculated according to the Arrhenius relationship

$$D = D_0 \exp\left(\frac{-\Delta E_a}{kT}\right) \quad (4)$$

where D_0 is the prefactor, *k* is the Boltzmann constant, and *T* is the temperature.

The conductivity was calculated based on the Nernst−Einstein equation

$$\sigma = \frac{nz^2F^2}{RT}D \quad (5)$$

https://doi.org/10.1021/acs.chemmater.3c00902
Chem. Mater. XXXX, XXX, XXX−XXX

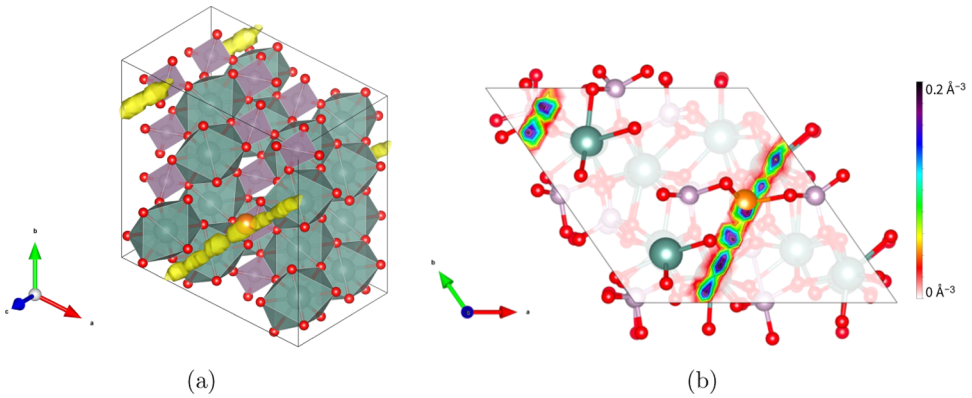

Figure 3. (a) Mg^{2+} nuclear density isosurface (yellow) in YPO_4 obtained from AIMD at 1500 K, where teal and purple polyhedrons represent YO_8 dodecahedrons and PO_4 tetrahedrons, respectively. (b) 2D view of the Mg^{2+} nuclear density map in the (001) plane.

where n is the density of mobile ions in the simulation cell, z is the charge carried by each mobile ion, F is the Faraday constant, D is the diffusion coefficient, R is the gas constant, and T is the temperature.

Synthesis and Characterization of $Na_{0.05}YSi_{0.05}P_{0.95}O_4$. YPO_4 and $Na_{0.05}YSi_{0.05}P_{0.95}O_4$ powders were prepared by solid-state synthesis with stoichiometric amounts of Y_2O_3 (99.9%), P_2O_5 (99.9%), Na_2O (97%), and SiO_2 (99.9%) precursors, all from Sigma-Aldrich. The mixed precursor powders were ball-milled at 300 rpm for 3 h and then heated at 900 °C for 36 h under air. YPO_4 and $Na_{0.05}YSi_{0.05}P_{0.95}O_4$ powder samples were characterized by X-ray diffraction (XRD) performed using a Rigaku MiniFlex 600 diffractometer with Cu Kα radiation. $Na_{0.05}YSi_{0.05}P_{0.95}O_4$ powders were cold-pressed to pellets with 2 metric tons of force using a die with a diameter of 6 mm for the conductivity measurement. Consecutive ball milling and sintering at 1100 °C were performed to improve the relative density of the pellet. The highest relative density obtained for the pellet was 78%.

The Na-ion conductivity was evaluated using electrochemical impedance spectroscopy (EIS) with indium metal as blocking electrodes. As-synthesized $Na_{0.05}YSi_{0.05}P_{0.95}O_4$ was sintered to a 2 mm thick pellet with a diameter of 6 mm. During the sintering, the powders were uniaxially compressed under a pressure of 300 MPa. The pellet was then sandwiched between two indium films and transferred into Bio-Logic leak-tight sample holders for EIS measurements. EIS measurements were performed using an EC-Lab Electrochemistry, SP300 (Bio-Logic). The measurements were conducted at the initial open-circuit voltage in the frequency range of 7 MHz to 100 mHz with the application of a 10 mV signal amplitude.

RESULTS AND DISCUSSION

$Na^+/Mg^{2+}/Ca^{2+}/Zn^{2+}$ Conduction in the Zircon-Type Framework. To assess the mobility of different carrier ions in the zircon-type framework, we used NEB calculations to obtain migration barriers in the dilute case for single interstitial hops. Based on the migration graph analysis, the most likely continuous pathway was identified to be constructed by a series of single hops between adjacent insertion sites that are octahedrally coordinated, as shown in Figure 1. We call these sites S_1 with a closer view of the channel in Figure 2a. The initial and end positions of the hop are symmetrically equivalent, and the length of the hop is about 1.5 Å. This 1D percolating pathway runs along the open channels, parallel to the YO_8−PO_4 edge-sharing chains, which has previously been identified as the most energetically favorable pathway for the diffusion of gases such as He and Ne in zircon crystals.[62,63]

Figure 2c shows the energy barriers along the minimum energy path (MEP) for Na^+, Mg^{2+}, Ca^{2+}, and Zn^{2+} migration in YPO_4. All carrier ions follow the same MEP passing through four-coordinated site S_2 at the saddle point (S_1−S_2−S_1 in Figure 2a). All investigated ions show low activation barriers, setting the stage for fast conduction of these carrier ions in the framework. We attribute the low migration barriers for multiple carrier species to the large open channels in the framework as well as the short distance between identical sites, resulting in a very gentle variation of the coordination environment along the pathway. As these features are shared by all members in the zircon family and the nonmobile cation species in the framework have limited effect on the ion mobility of carrier ions,[17,64,65] it is expected that comparable migration barriers can be achieved with Y and/or P substituted.

An extremely low energy barrier of 40 meV was observed for Zn^{2+} hops in YPO_4. As the migration barrier is closely related to the coordination environment of the conducting ion,[17] we attribute this low barrier to the 4-coordinated environment at the saddle point (S_2 in Figure 2a), which Zn^{2+} prefers.[66] To investigate other factors that may affect energy barriers for different carrier ions, we performed Voronoi tessellation analysis as implemented in Pymatgen[56,67] to determine the volume partitioned to the mobile ion site for both the endpoint and intermediate images along the migration pathway. The percentage change in mobile site volume is calculated as $(V_{S_1} - V_{S_2})/V_{S_1}$, where V_{S_1} and V_{S_2} represent the site volume when the mobile ion is in the stable state (S_1) and the intermediate state (S_2), respectively. The site volume change for different mobile species is shown in Figure 2b. A correlation between site volume change and the migration barrier is observed for Na^+, Mg^{2+}, and Ca^{2+}, which all exhibit higher, but still very low, migration barriers than Zn^{2+} along the same pathway. We note that Na^+, Mg^{2+}, and Ca^{2+} usually do not prefer 4-coordinate sites, and thus, a larger site volume change can lead to a larger variation of the energy, hence higher energy barriers.

The conduction of Li ions was also investigated in the same framework. Unlike other mobile cations in this study, we found the most stable site for Li^+ ions to be the 4-coordinated site in the channel (S_2), which constitutes the intermediate position for Na^+, Mg^{2+}, Ca^{2+}, and Zn^{2+}. As Li^+ prefers both 4- and 6-coordinated environments,[66] the site energy difference between S_1 and S_2 is relatively small, resulting in a very low energy barrier of 71 meV (Figure S2 in the Supporting Information).

AIMD simulations were conducted at 1500 K to further verify the primary pathway of ionic mobility in the zircon-type

https://doi.org/10.1021/acs.chemmater.3c00902
Chem. Mater. XXXX, XXX, XXX−XXX

Table 1. Decomposition Energies and Defect Formation Energies of Doped $A_xYM_yP_{1-y}O_4$

composition	carrier ion	x	dopant	y	E_{decomp} (meV/atom)	defect energy (eV)
$Na_{0.0208}YSi_{0.0208}P_{0.9792}O_4$	Na	0.0208	Si	0.0208	7	3.34
$Na_{0.0625}YSi_{0.0625}P_{0.9375}O_4$	Na	0.0625	Si	0.0625	19	-
$Ca_{0.0208}YAl_{0.0208}P_{0.9792}O_4$	Ca	0.0208	Al	0.0208	14	4.45
$Ca_{0.0208}YLa_{0.0208}P_{0.9792}O_4$	Ca	0.0208	La	0.0208	24	8.39
$Ca_{0.0208}YGa_{0.0208}P_{0.9792}O_4$	Ca	0.0208	Ga	0.0208	14	3.73
$Mg_{0.125}YSi_{0.25}P_{0.75}O_4$	Mg	0.1250	Si	0.2500	38	-
$Mg_{0.0625}YSi_{0.125}P_{0.875}O_4$	Mg	0.0625	Si	0.1250	21	-
$Mg_{0.0208}YAl_{0.0208}P_{0.9792}O_4$	Mg	0.0208	Al	0.0208	9	2.54
$Mg_{0.0208}YLa_{0.0208}P_{0.9792}O_4$	Mg	0.0208	La	0.0208	19	6.55
$Mg_{0.0208}YGa_{0.0208}P_{0.9792}O_4$	Mg	0.0208	Ga	0.0208	9	1.88
$Mg_{0.25}YSi_{0.5}P_{0.5}O_4$	Mg	0.2500	Si	0.5000	39	-
$Zn_{0.0208}YAl_{0.0208}P_{0.9792}O_4$	Zn	0.0208	Al	0.0208	8	2.03
$Zn_{0.0208}YGa_{0.0208}P_{0.9792}O_4$	Zn	0.0208	Ga	0.0208	9	1.36
$Zn_{0.0208}YLa_{0.0208}P_{0.9792}O_4$	Zn	0.0208	La	0.0208	18	5.85

framework. The nuclear density map of Mg^{2+} in pristine YPO_4 from AIMD (Figure 3) shows the percolating 1D movement of Mg ions parallel to the edge-sharing YO_8−PO_4 connecting chains in the zircon-type framework, consistent with the path information obtained by NEB calculations. The same pathway was observed for other carriers in YPO_4 (Figure S3 in the Supporting Information). The two-dimensional (2D) view of the Mg^{2+} nuclear density map shows the connected density spots between symmetrically equivalent neighboring carrier sites S_1, which confirms the MEP identified from NEB. Furthermore, no additional ionic mobility, either by framework ions or carrier ions, was observed from the MD simulations.

Phase Stability and Defect Formation Energy of Doped $A_xYM_yP_{1-y}O_4$. We evaluate the ability to introduce mobile ions by calculating the energy of materials that are modified with subvalent species. For YPO_4, we substitute M^{3+} or M^{4+} into P^{5+} sites to accommodate A^+ or A^{2+} carrier ions into the system. The energy of decomposition into stable products of various $A_xYM_yP_{1-y}O_4$ compositions and the formation energy of the A_i interstitial and M_P substitution defect pair in the dilute limit are calculated to evaluate the thermodynamic stability of $A_xYM_yP_{1-y}O_4$. The results are shown in Table 1. The decomposed products for each composition and their material IDs in the Materials Project database[57] are listed in Table S1 in the Supporting Information.

The relatively low decomposition energies across different compositions suggest that these doped structures are likely to be entropically stabilized at room temperature. At the same concentration, compositions with monovalent carrier ion A^+ and tetravalent M^{4+} show better stability than ones with A^{2+} and M^{3+}, which is likely due to the larger electrostatic potential change associated with A^{2+}−M^{3+} pairs. Among divalent mobile species, we find higher decomposition energy as well as larger defect formation energy for Ca^{2+} compared to cases with Mg^{2+} and Zn^{2+}. For trivalent dopant ions, higher instabilities and defect energies are found for ones with La^{3+} compared to Al^{3+} and Ga^{3+}, which may pose a challenge in the synthesis of these La-doped compositions. This can be attributed to the significantly larger size of lanthanum ions (117.2 pm) compared to the host ion P^{5+} (52 pm) as well as the two other dopants Al^{3+} (67.5 pm) and Ga^{3+} (76 pm), which result in larger local distortions. As the Si-doped YPO_4 with Na with a defect energy of 3.34 eV is successfully synthesized in this study, we expect compositions with dopant−carrier ion combinations exhibiting lower defect energies such as Mg−Al, Mg−Ga, Zn−Al, and Zn−Ga can potentially be synthesized.

Na Conduction in Si-Doped YPO_4. To investigate the cation mobility in the zircon-type framework when both carrier and dopant are present, NEB and AIMD calculations were performed to investigate Na^+ diffusion in Si-doped YPO_4 ($Na_{0.0625}YSi_{0.0625}P_{0.9375}O_4$). The 97-atom supercell was constructed with one Na^+ interstitial in the identified carrier ion site (Wyckoff position 16*f*) and one Si^{4+} substituted for a P^{5+}. Structures with the Na ion placed in each symmetrically unique carrier ion site in the cell (Na1 to Na5 in Figure 4a,b) were relaxed. NEB calculations were performed to evaluate the migration barriers of hops between the adjacent 16*f* sites, using four intermediate images for each hop. The lowest site energy was found for the Na1 and Na2 sites, two symmetrically equivalent sites that are closest to dopant Si. This reduction in site energy is attributed to the decreased Na^+−cation repulsion in replacing a P^{5+} with a Si^{4+}. A very low migration barrier of 80 meV was found between Na1 and Na2 sites. A larger (but

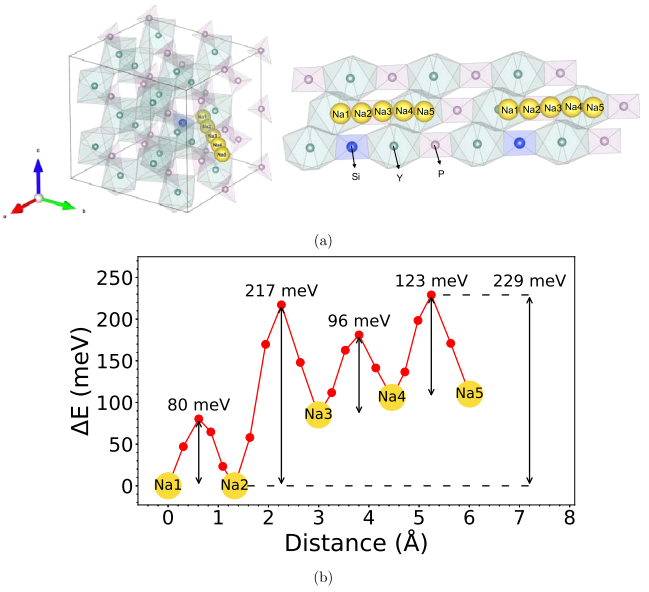

Figure 4. (a) Diffusion pathway from Na1 to Na5. The right figure shows two repeating units along the channel. (b) Migration energy along the connected NEB path from Na1 to Na5.

https://doi.org/10.1021/acs.chemmater.3c00902
Chem. Mater. XXXX, XXX, XXX−XXX

still relatively very small) activation energy of 217 meV is needed for the Na ion to "escape" from the Si dopant when moving from Na2 to Na3. When the Na−Si distance increases, the site energy increases continuously (from Na3 to Na4 to Na5) with Na−Si distances (see Figure 4). The activation energies for Na hops between these sites, further from the dopant, are similar to Na migration barriers in pristine YPO_4. Hence, the overall migration barrier for the 1D percolating pathway for Na at this composition is found to be 229 meV and is mainly determined by the lowering of the site energy near the dopant. Such "trapping" behavior, caused by the interaction between the carrier ion and the dopant, may increase the overall migration barriers as compared to pristine YPO_4 and will be further discussed in the following section. Nevertheless, the low activation barrier of 229 meV for $Na_{0.0625}YSi_{0.0625}P_{0.9375}O_4$ is comparable to those for well-known superionic Na-ion conductors such as polycrystalline β-alumina (0.26 eV[68]); NASICON-type structures with Mg-doping (0.25 eV[69]) and Sc-doping (0.26 eV[70]); sulfides like Sn-doped cubic Na_3PS_4 (0.17 eV[71]) and tetragonal Na_3SbS_4 (0.25 eV[72]); and antiperovskite-type Na_3OCl (0.42 eV[73]).

AIMD simulations were performed to evaluate the diffusivity and conductivity of Na^+ in $Na_{0.0625}YSi_{0.0625}P_{0.9375}O_4$. Figure 5

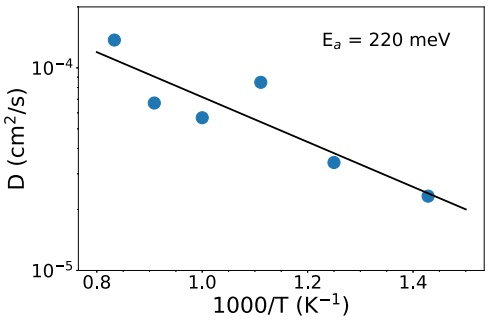

Figure 5. Arrhenius plot of Na^+ diffusivity in $Na_{0.0625}YSi_{0.0625}P_{0.9375}O_4$ obtained from AIMD.

shows the Arrhenius plot of the temperature-dependent Na^+ diffusivity obtained from AIMD. The mean-squared displacement of Na vs time at each temperature is shown in Figure S5 in the Supporting Information. The activation energy in the temperature range from 700 to 1200 K is 220 ± 55 meV, which is consistent with NEB calculations above. Despite the very low Na^+ concentration in the system that can limit the overall conductivity according to eq 5, we estimate good Na^+ conductivity of 0.99 mS/cm $Na_{0.0625}YSi_{0.0625}P_{0.9375}O_4$ when extrapolating to 300 K, assuming that the Arrhenius relationship applies into the low-temperature region. This is a notable feature of the zircon structure that contrasts with many current high-performance conductors; high concentrations of the mobile ion are evidently not necessary to achieve high conductivities. While higher conductivity may potentially be achieved with more Na incorporated into the system with accordingly increased dopant concentration, it may also present exacerbated synthesis conditions as we expect a higher decomposition energy of the target material toward the impurity phases.

$Na_{0.05}YSi_{0.05}P_{0.95}O_4$ was successfully synthesized through a solid-state method. The XRD patterns of YPO_4 and $Na_{0.05}YSi_{0.05}P_{0.95}O_4$ are shown in Figure 6. To confirm that no structural changes took place upon densification, we also

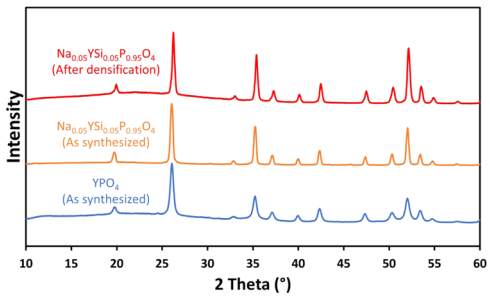

Figure 6. XRD profiles of YPO_4 and $Na_{0.05}YSi_{0.05}P_{0.95}O_4$.

present the XRD pattern of $Na_{0.05}YSi_{0.05}P_{0.95}O_4$ after densification. Rietveld refinement of XRD patterns for YPO_4 and $Na_{0.05}YSi_{0.05}P_{0.95}O_4$ are shown in Figures S6 and S7 in the Supporting Information, with R_{wp} = 6.87% and R_{wp} = 4.12%, respectively. In order to check the presence of Na in the sample, energy-dispersive spectrometry (EDS) analysis was performed after densification. Figure S8 in the Supporting Information shows the compositional distribution of Y, P, Si, and Na in the sample. EDS data is collected from different locations from the sample, and the average composition is found to be $Na_{0.045}Y_{0.9925}Si_{0.048}P_{0.95}O_4$.

To measure the conductivity, the $Na_{0.05}YSi_{0.05}P_{0.95}O_4$ powders were cold-pressed into a pellet for the electrochemical impedance spectroscopy (EIS) experiment. However, the pellet's highest relative density achieved was only 78%, leading to unreliable conductivity measurement from EIS (Figure S1 in the Supporting Information) due to high grain boundary resistance and pores blocking the conduction pathways. The pellet was broken after the measurement, which also suggests the high porosity of the sample, which leads to low conductivity. Such an effect of poor densification on conductivity is commonly observed in other ionic conductors.[74,75] Moreover, for 1D conductors, the diffusion channels can be easily blocked with defects and impurities.[76,77] Future research should focus on optimizing the synthesis and sintering conditions to minimize these effects.

Dopant−Carrier Association in Doped YPO_4. When both dopant ion and carrier ion are present in the system, the subvalent dopant and the positively charged carrier can form defect pairs introduced by electrostatic or strain interactions.[78,79] As a result, carrier ions may be trapped by the dopant, reducing the long-range transport and overall carrier ion mobility. To investigate the dopant−carrier association behavior in YPO_4, we calculated the dopant−carrier binding energy using a 2 × 2 × 3 supercell of the conventional unit cell, consisting of 48 formula units. The binding energy is calculated as $E_b = E_p - E_i$, where E_p is the total energy of the system where the dopant ion is doped into the P site closest to the carrier ion and E_i is the total energy of the system where the dopant and the carrier are isolated with at least 11 Å distance between them. The higher the binding energy, the more strongly bound the carrier ion to the dopant ion and less likely to move past it.

Figure 7 shows the binding energy of divalent carrier and trivalent dopant pairs versus the ionic radii of the dopant. We investigated the cases when the dopant is either Ga^{3+}, La^{3+}, or Al^{3+} and the carrier ion is either Ca^{2+}, Mg^{2+}, or Zn^{2+}. We observe high binding energies for all dopant−carrier pairs, which suggests a significant trapping effect of the carrier ions by the dopant ions. Zn^{2+} shows higher binding energy than

https://doi.org/10.1021/acs.chemmater.3c00902
Chem. Mater. XXXX, XXX, XXX−XXX

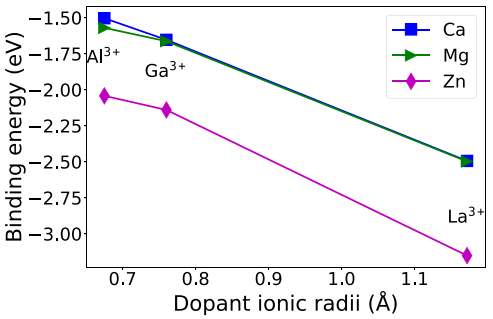

Figure 7. Dopant−carrier binding energy vs the ionic radius of the dopant ion.

Ca^{2+} and Mg^{2+} for equivalent dopants. Clear correlations between the binding energy and the ionic radius of the dopant ion are observed for all carrier ions. As these dopant ions all exhibit larger ionic radii than P^{5+}, the higher binding energy with larger dopant ions can be explained by the increased elastic strain effects due to the increased ion size mismatch between the dopant and the host ion.[78]

We further analyzed the trapping behavior when the concentration of carriers and dopants were increased. The site energy of Mg^{2+} occupying different sites in $Mg_{0.25}YSi_{0.5}P_{0.5}O_4$ was calculated and is shown in Figure S4 in the Supporting Information. Indeed, at this composition, a large barrier of about 1.5 eV was found for Mg^{2+} to move from the Si-surrounded site, suggesting very low Mg^{2+} mobility.

The analysis of dopant−carrier association in doped YPO_4 sheds light on the challenge of realizing the potential of zircon compounds as Ca/Mg/Zn ionic conductors with the low activation energies predicted in pristine YPO_4. Finding ways to lower the binding energy between the carrier ion and the dopant ion appears essential. We hypothesize that it may be addressed by a thoughtful selection of dopant ions with similar ionic size to the A or B sites in the host ABO_4, which may reduce the dopant−carrier binding energy and facilitate mobility.

CONCLUSIONS

In this work, we investigated the conduction of monovalent Na^+ and divalent Ca^{2+}, Mg^{2+}, and Zn^{2+} in YPO_4 with a zircon-type crystal structural framework. We found remarkably low migration barriers for both monovalent and a broad range of divalent cations through a 1D channel of adjacent, distorted octahedral sites in YPO_4. Furthermore, we note that the zircon framework supports intrinsically low activation barriers, even at low mobile ion concentrations, a rare quality among candidate conductor structure families. We attribute the uncommonly low migration barriers in the zircon-type framework for multiple mobile species to the relatively spacious, open channels formed by the directly connected and slightly distorted octahedra, which results in a smooth variation of the coordination environment along the channel. For different mobile species, the energy barrier is affected by the local environment preference of the mobile ion as well as the site volume change along the migration pathway. By analyzing the phase stability of doped YPO_4 and the defect formation energy, we found that doped zircons are likely to be synthesized. Specifically, we predicted $Na_{0.0625}YSi_{0.0625}P_{0.9375}O_4$ to be a promising fast Na conductor with Na^+ conductivity of 0.99 mS/cm at 300 K and a very low activation energy of 220 meV, even in the dilute carrier concentration regime. In agreement with estimated low decomposition energies, $Na_{0.05}YSi_{0.05}P_{0.95}O_4$ powders were successfully synthesized by a solid-state method and confirmed to crystallize in the zircon structure. Challenges in achieving high-density pellets limit the reliability of the conductivity measurements.

We analyzed the dopant−carrier association in doped YPO_4, which often constitutes an obstacle to achieving fast conduction, especially in the case of divalent cations. With the insights and guidance on YPO_4 provided in this study, further research efforts through both experimental and computational approaches are encouraged, particularly in identifying optimal zircon compositions with comparable barriers, lowered dopant−carrier binding energies, and improved conductivity to fully realize fast, multispecies conduction within the large family of zircon compounds.

ASSOCIATED CONTENT

Supporting Information

The Supporting Information is available free of charge at https://pubs.acs.org/doi/10.1021/acs.chemmater.3c00902.

Nyquist impedance plots of the $Na_{0.05}YSi_{0.05}P_{0.95}O_4$ pellet; energy profile along the Li^+ diffusion pathway $S_1-S_2-S_1-S_2$ in the channel; decomposed products of $A_xYM_yP_{1-y}O_4$; nuclear density plots of Li, Na, Zn, and Ca in YPO_4 obtained from AIMD at 1500 K; structure and site energies of $Mg_{0.25}YSi_{0.5}P_{0.5}O_4$; mean-squared displacement of Na in $Na_{0.0625}YSi_{0.0625}P_{0.9375}O_4$ vs time; Rietveld refinement of XRD patterns for YPO_4 and $Na_{0.05}YSi_{0.05}P_{0.95}O_4$; and SEM and elemental mapping images of P, Na, Si, and Y for $Na_{0.05}YSi_{0.05}P_{0.95}O_4$ (PDF)

AUTHOR INFORMATION

Corresponding Author

Kristin A. Persson − *Materials Sciences Division, Lawrence Berkeley National Laboratory, Berkeley, California 94720, United States; Material Science and Engineering Department, University of California, Berkeley, California 94704, United States; Molecular Foundry, Lawrence Berkeley National Laboratory, Berkeley, California 94720, United States;* orcid.org/0000-0003-2495-5509; Email: kapersson@lbl.gov

Authors

Qian Chen − *Materials Sciences Division, Lawrence Berkeley National Laboratory, Berkeley, California 94720, United States;* orcid.org/0009-0009-3557-0744

Dogancan Sari − *Material Science and Engineering Department, University of California, Berkeley, California 94704, United States*

Ann Rutt − *Materials Sciences Division, Lawrence Berkeley National Laboratory, Berkeley, California 94720, United States; Material Science and Engineering Department, University of California, Berkeley, California 94704, United States;* orcid.org/0000-0001-6534-454X

Jiyoon Kim − *Materials Sciences Division, Lawrence Berkeley National Laboratory, Berkeley, California 94720, United States; Material Science and Engineering Department, University of California, Berkeley, California 94704, United States;* orcid.org/0000-0002-0383-1198

Gerbrand Ceder − *Materials Sciences Division, Lawrence Berkeley National Laboratory, Berkeley, California 94720,*

United States; Material Science and Engineering Department, University of California, Berkeley, California 94704, United States; orcid.org/0000-0001-9275-3605

Complete contact information is available at: https://pubs.acs.org/10.1021/acs.chemmater.3c00902

Notes

The authors declare no competing financial interest.

■ ACKNOWLEDGMENTS

This work was supported by the Joint Center for Energy Storage Research (JCESR), an Energy Innovation Hub funded by the U.S. Department of Energy, Office of Science, Basic Energy Sciences. This research used resources of the National Energy Research Scientific Computing Center (NERSC), a U.S. Department of Energy Office of Science User Facility located at Lawrence Berkeley National Laboratory, operated under Contract No. DE-AC02-05CH11231. The work of D.S. was supported by a Fulbright Program grant sponsored by the Bureau of Educational and Cultural Affairs of the United States Department of State and administered by the Institute of International Education.

■ REFERENCES

(1) Harlow, J. E.; Ma, X.; Li, J.; Logan, E.; Liu, Y.; Zhang, N.; Ma, L.; Glazier, S. L.; Cormier, M. M. E.; Genovese, M.; Buteau, S.; Cameron, A.; Stark, J. E.; Dahn, J. R. A Wide Range of Testing Results on an Excellent Lithium-Ion Cell Chemistry to be used as Benchmarks for New Battery Technologies. *J. Electrochem. Soc.* **2019**, *166*, No. A3031.

(2) Tian, Y.; Zeng, G.; Rutt, A.; Shi, T.; Kim, H.; Wang, J.; Koettgen, J.; Sun, Y.; Ouyang, B.; Chen, T.; Lun, Z.; Rong, Z.; Persson, K.; Ceder, G. Promises and Challenges of Next-Generation "Beyond Li-ion" Batteries for Electric Vehicles and Grid Decarbonization. *Chem. Rev.* **2021**, *121*, 1623−1669.

(3) Palomares, V.; Serras, P.; Villaluenga, I.; Hueso, K. B.; Carretero-González, J.; Rojo, T. Na-ion batteries, recent advances and present challenges to become low cost energy storage systems. *Energy Environ. Sci.* **2012**, *5*, 5884−5901.

(4) Goikolea, E.; Palomares, V.; Wang, S.; de Larramendi, I. R.; Guo, X.; Wang, G.; Rojo, T. Na-ion batteries—approaching old and new challenges. *Adv. Energy Mater.* **2020**, *10*, No. 2002055.

(5) Liang, Y.; Dong, H.; Aurbach, D.; Yao, Y. Current status and future directions of multivalent metal-ion batteries. *Nat. Energy* **2020**, *5*, 646−656.

(6) Gummow, R. J.; Vamvounis, G.; Kannan, M. B.; He, Y. Calcium-ion batteries: current state-of-the-art and future perspectives. *Adv. Mater.* **2018**, *30*, No. 1801702.

(7) Saha, P.; Datta, M. K.; Velikokhatnyi, O. I.; Manivannan, A.; Alman, D.; Kumta, P. N. Rechargeable magnesium battery: Current status and key challenges for the future. *Prog. Mater. Sci.* **2014**, *66*, 1−86.

(8) Tang, B.; Shan, L.; Liang, S.; Zhou, J. Issues and opportunities facing aqueous zinc-ion batteries. *Energy Environ. Sci.* **2019**, *12*, 3288−3304.

(9) Hull, S. Superionics: crystal structures and conduction processes. *Rep. Prog. Phys.* **2004**, *67*, No. 1233.

(10) Ohno, S.; Banik, A.; Dewald, G. F.; Kraft, M. A.; Krauskopf, T.; Minafra, N.; Till, P.; Weiss, M.; Zeier, W. G. Materials design of ionic conductors for solid state batteries. *Prog. Energy* **2020**, *2*, No. 022001.

(11) Wang, Y.; Richards, W. D.; Ong, S. P.; Miara, L. J.; Kim, J. C.; Mo, Y.; Ceder, G. Design principles for solid-state lithium superionic conductors. *Nat. Mater.* **2015**, *14*, 1026−1031.

(12) He, X.; Bai, Q.; Liu, Y.; Nolan, A. M.; Ling, C.; Mo, Y. Crystal structural framework of lithium super-ionic conductors. *Adv. Energy Mater.* **2019**, *9*, No. 1902078.

(13) Bachman, J. C.; Muy, S.; Grimaud, A.; Chang, H.-H.; Pour, N.; Lux, S. F.; Paschos, O.; Maglia, F.; Lupart, S.; Lamp, P.; Giordano, L.; Shao-Horn, Y. Inorganic Solid-State Electrolytes for Lithium Batteries: Mechanisms and Properties Governing Ion Conduction. *Chem. Rev.* **2016**, *116*, 140−162.

(14) Jun, K.; Sun, Y.; Xiao, Y.; Zeng, Y.; Kim, R.; Kim, H.; Miara, L. J.; Im, D.; Wang, Y.; Ceder, G. Lithium superionic conductors with corner-sharing frameworks. *Nat. Mater.* **2022**, *21*, 924−931.

(15) Xiao, Y.; Jun, K.; Wang, Y.; Miara, L. J.; Tu, Q.; Ceder, G. Lithium oxide superionic conductors inspired by garnet and NASICON structures. *Adv. Energy Mater.* **2021**, *11*, No. 2101437.

(16) Ong, S. P.; Chevrier, V. L.; Hautier, G.; Jain, A.; Moore, C.; Kim, S.; Ma, X.; Ceder, G. Voltage, stability and diffusion barrier differences between sodium-ion and lithium-ion intercalation materials. *Energy Environ. Sci.* **2011**, *4*, 3680−3688.

(17) Rong, Z.; Malik, R.; Canepa, P.; Sai Gautam, G.; Liu, M.; Jain, A.; Persson, K.; Ceder, G. Materials Design Rules for Multivalent Ion Mobility in Intercalation Structures. *Chem. Mater.* **2015**, *27*, 6016−6021.

(18) Yao, Y.-F. Y.; Kummer, J. Ion exchange properties of and rates of ionic diffusion in beta-alumina. *J. Inorg. Nucl. Chem.* **1967**, *29*, 2453−2475.

(19) Farrington, G. C.; Dunn, B. Divalent beta "-aluminas: high conductivity solid electrolytes for divalent cations. *Solid State Ionics* **1982**, *7*, 267−281.

(20) Seevers, R.; DeNuzzio, J.; Farrington, G.; Dunn, B. Ion transport in Ca2+, Sr2+, Ba2+, and Pb2+ beta "aluminas. *J. Solid State Chem.* **1983**, *50*, 146−152.

(21) Chernova, N. A.; Roppolo, M.; Dillon, A. C.; Whittingham, M. S. Layered vanadium and molybdenum oxides: batteries and electrochromics. *J. Mater. Chem.* **2009**, *19*, 2526−2552.

(22) Xu, X.; Xiong, F.; Meng, J.; Wang, X.; Niu, C.; An, Q.; Mai, L. Vanadium-based nanomaterials: a promising family for emerging metal-ion batteries. *Adv. Funct. Mater.* **2020**, *30*, No. 1904398.

(23) Lu, Y.; Zhu, T.; van den Bergh, W.; Stefik, M.; Huang, K. A High Performing Zn-Ion Battery Cathode Enabled by In Situ Transformation of V2O5 Atomic Layers. *Angew. Chem.* **2020**, *132*, 17152−17159.

(24) Wan, L. F.; Incorvati, J. T.; Poeppelmeier, K. R.; Prendergast, D. Building a fast lane for Mg diffusion in α-MoO3 by fluorine doping. *Chem. Mater.* **2016**, *28*, 6900−6908.

(25) Xiong, T.; Zhang, Y.; Wang, Y.; Lee, W. S. V.; Xue, J. Hexagonal MoO3 as a zinc intercalation anode towards zinc metal-free zinc-ion batteries. *J. Mater. Chem. A* **2020**, *8*, 9006−9012.

(26) Chae, M. S.; Kwak, H. H.; Hong, S.-T. Calcium molybdenum bronze as a stable high-capacity cathode material for calcium-ion batteries. *ACS Appl. Energy Mater.* **2020**, *3*, 5107−5112.

(27) Whittingham, M. S. Chemistry of intercalation compounds: Metal guests in chalcogenide hosts. *Prog. Solid State Chem.* **1978**, *12*, 41−99.

(28) Samad, A.; Shafique, A.; Shin, Y.-H. Adsorption and diffusion of mono, di, and trivalent ions on two-dimensional TiS2. *Nanotechnology* **2017**, *28*, No. 175401.

(29) Tchitchekova, D. S.; Ponrouch, A.; Verrelli, R.; Broux, T.; Frontera, C.; Sorrentino, A.; Barde, F.; Biskup, N.; Arroyo-de Dompablo, M. E.; Palacin, M. R. Electrochemical intercalation of calcium and magnesium in TiS2: fundamental studies related to multivalent battery applications. *Chem. Mater.* **2018**, *30*, 847−856.

(30) Goodenough, J. B.; Hong, H.-P.; Kafalas, J. Fast Na+-ion transport in skeleton structures. *Mater. Res. Bull.* **1976**, *11*, 203−220.

(31) Nomura, K.; Ikeda, S.; Ito, K.; Einaga, H. Framework structure, phase transition and ionic conductivity of MgZr4(PO4)6 and ZnZr4(PO4)6. *J. Electroanal. Chem.* **1992**, *326*, 351−356.

(32) Nomura, K.; Ikeda, S.; Ito, K.; Einaga, H. Framework structure, phase transition, and transport properties in MIIZr4 (PO4) 6 compounds (MII= Mg, Ca, Sr, Ba, Mn, Co, Ni, Zn, Cd, and Pb). *Bull. Chem. Soc. Jpn.* **1992**, *65*, 3221−3227.

(33) Jian, Z.; Hu, Y.-S.; Ji, X.; Chen, W. NASICON-Structured Materials for Energy Storage. *Adv. Mater* **2017**, *29*, No. 1601925.

(34) Tamura, S.; Yamane, M.; Hoshino, Y.; Imanaka, N. Highly conducting divalent Mg2+ cation solid electrolytes with well-ordered three-dimensional network structure. *J. Solid State Chem.* **2016**, *235*, 7−11.
(35) Jeon, B.; Heo, J. W.; Hyoung, J.; Kwak, H. H.; Lee, D. M.; Hong, S.-T. Reversible calcium-ion insertion in NASICON-type NaV2 (PO4) 3. *Chem. Mater.* **2020**, *32*, 8772−8780.
(36) Li, G.; Yang, Z.; Jiang, Y.; Jin, C.; Huang, W.; Ding, X.; Huang, Y. Towards polyvalent ion batteries: a zinc-ion battery based on NASICON structured Na3V2 (PO4) 3. *Nano Energy* **2016**, *25*, 211−217.
(37) Smeu, M.; Hossain, M. S.; Wang, Z.; Timoshevskii, V.; Bevan, K. H.; Zaghib, K. Theoretical investigation of Chevrel phase materials for cathodes accommodating Ca2+ ions. *J. Power Sources* **2016**, *306*, 431−436.
(38) Mei, L.; Xu, J.; Wei, Z.; Liu, H.; Li, Y.; Ma, J.; Dou, S. Chevrel phase Mo6T8 (T= S, Se) as electrodes for advanced energy storage. *Small* **2017**, *13*, No. 1701441.
(39) Levi, E.; Gershinsky, G.; Aurbach, D.; Isnard, O. Crystallography of chevrel phases, MMo6T8 (M= Cd, Na, Mn, and Zn, T= S, Se) and their cation mobility. *Inorg. Chem.* **2009**, *48*, 8751−8758.
(40) Levi, E.; Gershinsky, G.; Aurbach, D.; Isnard, O.; Ceder, G. New insight on the unusually high ionic mobility in chevrel phases. *Chem. Mater.* **2009**, *21*, 1390−1399.
(41) Aurbach, D.; Lu, Z.; Schechter, A.; Gofer, Y.; Gizbar, H.; Turgeman, R.; Cohen, Y.; Moshkovich, M.; Levi, E. Prototype systems for rechargeable magnesium batteries. *Nature* **2000**, *407*, 724−727.
(42) He, X.; Zhu, Y.; Mo, Y. Origin of fast ion diffusion in superionic conductors. *Nat. Commun.* **2017**, *8*, No. 15893.
(43) Xu, M.; Park, M. S.; Lee, J. M.; Kim, T. Y.; Park, Y. S.; Ma, E. Mechanisms of Li+ transport in garnet-type cubic Li 3+ x La 3 M 2 O 12 (M= Te, Nb, Zr). *Phys. Rev. B* **2012**, *85*, No. 052301.
(44) Finch, R. J.; Hanchar, J. M. Structure and Chemistry of Zircon and Zircon-Group Minerals. *Rev. Mineral. Geochem.* **2003**, *53*, 1−25.
(45) Crocombette, J.-P. Theoretical study of point defects in crystalline zircon. *Phys. Chem. Miner.* **1999**, *27*, 138−143.
(46) Gao, F.; Xiao, H. Y.; Zhou, Y.; Devanathan, R.; Hu, S. Y.; Li, Y.; Sun, X.; Khaleel, M. A. Ab initio study of defect properties in YPO4. *Comput. Mater. Sci.* **2012**, *54*, 170−175.
(47) Cutts, G. L.; Hriljac, J. A.; Read, M. S. Derivation of Transferable Pair Potentials and the Calculation of Intrinsic Defect Properties for Xenotime. *J. Phys. Chem. C* **2018**, *122*, 25617−25627.
(48) Esaka, T.; Kobayashi, Y.; Obata, H.; Iwahara, H. Cation conduction in zircon-type solid solution based on YPO4. *Solid State Ionics* **1989**, *34*, 287−291.
(49) Amezawa, K.; Tomii, Y.; Yamamoto, N. High temperature protonic conduction in Ca-doped YPO4. *Solid State Ionics* **2003**, *162−163*, 175−180.
(50) Shen, J.-X.; Horton, M.; Persson, K. A. A charge-density-based general cation insertion algorithm for generating new Li-ion cathode materials. *npj Comput. Mater.* **2020**, *6*, No. 167.
(51) Rutt, A.; Sari, D.; Chen, Q.; Kim, J.; Ceder, G.; Persson, K. A. A Novel Structural Motif to Promote Mg-ion Mobility: Investigating ABO4 Zircons as Magnesium Intercalation Cathodes. *ACS Appl. Mater. Interfaces* **2023**, *15*, 34983−34991.
(52) Kresse, G.; Furthmüller, J. Efficient iterative schemes for ab initio total-energy calculations using a plane-wave basis set. *Phys. Rev. B* **1996**, *54*, 11169−11186.
(53) Blöchl, P. E. Projector augmented-wave method. *Phys. Rev. B* **1994**, *50*, 17953−17979.
(54) Perdew, J. P.; Burke, K.; Ernzerhof, M. Generalized Gradient Approximation Made Simple. *Phys. Rev. Lett.* **1996**, *77*, 3865−3868.
(55) Shen, J.-X.; Li, H. H.; Rutt, A.; Horton, M. K.; Persson, K. A. Topological graph-based analysis of solid-state ion migration. *npj Comput. Mater.* **2023**, *9*, No. 99.
(56) Ong, S. P.; Richards, W. D.; Jain, A.; Hautier, G.; Kocher, M.; Cholia, S.; Gunter, D.; Chevrier, V. L.; Persson, K. A.; Ceder, G. Python Materials Genomics (pymatgen): A robust, open-source python library for materials analysis. *Comput. Mater. Sci.* **2013**, *68*, 314−319.
(57) Jain, A.; Ong, S. P.; Hautier, G.; Chen, W.; Richards, W. D.; Dacek, S.; Cholia, S.; Gunter, D.; Skinner, D.; Ceder, G.; Persson, K. A. Commentary: The Materials Project: A materials genome approach to accelerating materials innovation. *APL Mater.* **2013**, *1*, No. 011002.
(58) Ong, S. P.; Wang, L.; Kang, B.; Ceder, G. Li-Fe-P-O2 phase diagram from first principles calculations. *Chem. Mater.* **2008**, *20*, 1798−1807.
(59) Henkelman, G.; Uberuaga, B. P.; Jónsson, H. A climbing image nudged elastic band method for finding saddle points and minimum energy paths. *J. Chem. Phys.* **2000**, *113*, 9901−9904.
(60) Henkelman, G.; Jónsson, H. Improved tangent estimate in the nudged elastic band method for finding minimum energy paths and saddle points. *J. Chem. Phys.* **2000**, *113*, 9978−9985.
(61) Cheng, J.; Sivonxay, E.; Persson, K. A. Evaluation of amorphous oxide coatings for high-voltage Li-ion battery applications using a first-principles framework. *ACS Appl. Mater. Interfaces* **2020**, *12*, 35748−35756.
(62) Gautheron, C.; Djimbi, D. M.; Roques, J.; Balout, H.; Ketcham, R. A.; Simoni, E.; Pik, R.; Seydoux-Guillaume, A.-M.; Tassan-Got, L. A multi-method, multi-scale theoretical study of He and Ne diffusion in zircon. *Geochim. Cosmochim. Acta* **2020**, *268*, 348−367.
(63) Bengtson, A.; Ewing, R. C.; Becker, U. He diffusion and closure temperatures in apatite and zircon: A density functional theory investigation. *Geochim. Cosmochim. Acta* **2012**, *86*, 228−238.
(64) Wang, Y.; Richards, W. D.; Ong, S. P.; Miara, L. J.; Kim, J. C.; Mo, Y.; Ceder, G. Design principles for solid-state lithium superionic conductors. *Nat. Mater.* **2015**, *14*, 1026−1031.
(65) Kang, K.; Ceder, G. Factors that affect Li mobility in layered lithium transition metal oxides. *Phys. Rev. B* **2006**, *74*, No. 094105.
(66) Brown, I. D. What factors determine cation coordination numbers? *Acta Crystallogr., Sect. B: Struct. Sci.* **1988**, *44*, 545−553.
(67) O'Keeffe, M. A proposed rigorous definition of coordination number. *Acta Crystallogr., Sect. A: Cryst. Phys., Diffr., Theor. Gen. Crystallogr.* **1979**, *35*, 772−775.
(68) Hooper, A. A study of the electrical properties of single-crystal and polycrystalline β-alumina using complex plane analysis. *J. Phys. D: Appl. Phys.* **1977**, *10*, 1487.
(69) Song, S.; Duong, H. M.; Korsunsky, A. M.; Hu, N.; Lu, L. A Na + superionic conductor for room-temperature sodium batteries. *Sci. Rep.* **2016**, *6*, No. 32330.
(70) Ma, Q.; Guin, M.; Naqash, S.; Tsai, C.-L.; Tietz, F.; Guillon, O. Scandium-substituted Na3Zr2 (SiO4) 2 (PO4) prepared by a solution-assisted solid-state reaction method as sodium-ion conductors. *Chem. Mater.* **2016**, *28*, 4821−4828.
(71) Zhu, Z.; Chu, I.-H.; Deng, Z.; Ong, S. P. Role of Na+ Interstitials and Dopants in Enhancing the Na+ Conductivity of the Cubic Na3PS4 Superionic Conductor. *Chem. Mater.* **2015**, *27*, 8318−8325.
(72) Zhang, L.; Zhang, D.; Yang, K.; Yan, X.; Wang, L.; Mi, J.; Xu, B.; Li, Y. Vacancy-Contained Tetragonal Na3SbS4 Superionic Conductor. *Adv. Sci.* **2016**, *3*, No. 1600089.
(73) Wan, T. H.; Lu, Z.; Ciucci, F. A first principle study of the phase stability, ion transport and substitution strategy for highly ionic conductive sodium antipervoskite as solid electrolyte for sodium ion batteries. *J. Power Sources* **2018**, *390*, 61−70.
(74) Rosero-Navarro, N. C.; Yamashita, T.; Miura, A.; Higuchi, M.; Tadanaga, K. Effect of sintering additives on relative density and Li-ion conductivity of Nb-doped Li7La3ZrO12Solid electrolyte. *J. Am. Ceram. Soc.* **2017**, *100*, 276−285.
(75) Doux, J.-M.; Yang, Y.; Tan, D. H. S.; Nguyen, H.; Wu, E. A.; Wang, X.; Banerjee, A.; Meng, Y. S. Pressure effects on sulfide electrolytes for all solid-state batteries. *J. Mater. Chem. A* **2020**, *8*, 5049−5055.
(76) Malik, R.; Burch, D.; Bazant, M.; Ceder, G. Particle size dependence of the ionic diffusivity. *Nano Lett.* **2010**, *10*, 4123−4127.

https://doi.org/10.1021/acs.chemmater.3c00902
Chem. Mater. XXXX, XXX, XXX−XXX

(77) Morgan, D.; Van der Ven, A.; Ceder, G. Li Conductivity in Li x MPO 4 (M = Mn, Fe, Co, Ni) Olivine Materials. *Electrochem. Solid-State Lett.* **2003**, *7*, No. A30.
(78) Kilner, J. A. Fast oxygen transport in acceptor doped oxides. *Solid State Ionics* **2000**, *129*, 13−23.
(79) Islam, M. S.; Davies, R. A. Atomistic study of dopant site-selectivity and defect association in the lanthanum gallate perovskite. *J. Mater. Chem.* **2004**, *14*, 86−93.

https://doi.org/10.1021/acs.chemmater.3c00902
Chem. Mater. XXXX, XXX, XXX−XXX